





To jump or not to jump: Adhesion and viscous dissipation dictate the detachment of coalescing wall-attached bubbles

Çayan Demirkır , Rui Yang , Aleksandr Bashkatov , and Vatsal Sanjay 

Physics of Fluids Department, Max Planck Center Twente for Complex Fluid Dynamics, and J. M. Burgers Center for Fluid Dynamics, University of Twente, P.O. Box 217, 7500AE Enschede, Netherlands

Detlef Lohse 

Physics of Fluids Department, Max Planck Center Twente for Complex Fluid Dynamics, and J. M. Burgers Center for Fluid Dynamics, University of Twente, P.O. Box 217, 7500AE Enschede, Netherlands and Max Planck Institute for Dynamics and Self-Organisation, Am Fassberg 17, 37077 Göttingen, Germany

Dominik Krug *

Physics of Fluids Department, Max Planck Center Twente for Complex Fluid Dynamics, and J. M. Burgers Center for Fluid Dynamics, University of Twente, P.O. Box 217, 7500AE Enschede, Netherlands and Institute of Aerodynamics, RWTH Aachen University, Wüllnerstrasse 5a, 52062 Aachen, Germany



(Received 9 January 2025; accepted 27 October 2025; published 8 December 2025)

Bubble coalescence can promote bubble departure at much smaller bubble sizes than those required for buoyancy-driven detachment. This can critically enhance the efficiency of gas-evolving electrochemical processes, such as water electrolysis. In this study, we integrate high-speed imaging experiments and direct numerical simulations to dissect how and under which conditions bubble coalescence on surfaces leads to detachment. Our transparent electrode experiments provide insights into contact line dynamics, demonstrating that the bubble neck generally does not contact the surface during coalescence. We reveal that whether coalescence leads to bubble departure or not is determined by the balance between surface energy, adhesion forces, and viscous dissipation. For the previously unexplored regime at low effective Ohnesorge number, a measure of viscosity that incorporates the effect of asymmetry between the coalescing bubbles, we identify a critical dimensionless adhesion energy threshold of $\approx 15\%$ of the released surface energy, below which bubbles typically detach. We develop a global energy balance model that successfully predicts coalescence outcomes across diverse experimental conditions.

DOI: [10.1103/nq3w-57gg](https://doi.org/10.1103/nq3w-57gg)

I. INTRODUCTION

Coalescence events are ubiquitous and drive numerous natural and industrial phenomena, from gas exchange in aquatic ecosystems [1,2] to raindrop formation [3] and chemical reactors [4]. In particular, by initiating the departure of surface-attached bubbles at smaller sizes and through the release of surface energy rather than relying on buoyancy, coalescence can affect the efficiency of

*Contact author: d.krug@aia.rwth-aachen.de

Published by the American Physical Society under the terms of the [Creative Commons Attribution 4.0 International](https://creativecommons.org/licenses/by/4.0/) license. Further distribution of this work must maintain attribution to the author(s) and the published article's title, journal citation, and DOI.

many industrially relevant processes, such as boiling and gas-evolving chemical reactions [5,6]. In light of the ongoing energy transition, there is particular interest in the role of bubbles in electrochemical systems [7,8], where mitigating bubble effects is considered key to enabling cost-effective production of green hydrogen [9]. Bubbles play a critical role in these systems, as they can block the active surface area, obstruct ion transport pathways, and generally affect the mass transport [10,11]. Controlling the bubble population via coalescence-induced detachment is attractive, since it enables earlier detachment compared to the buoyancy limits of the parent bubbles [12–16] without external actuation. The concept has proven effective in increasing the performance in a microelectrode model [17]. However, applying this approach to practical systems requires understanding the conditions under which coalescence triggers departure, which is the focus of this work.

Coalescence of wall-attached bubbles can result in “jumping,” where the merged bubble detaches, or “sticking,” when it remains attached. During the event, surface energy is transformed into kinetic energy. The associated viscous dissipation differs fundamentally between droplets and bubbles coalescence. For droplets, viscous losses occur within the confined liquid volume with well-defined characteristic scales [18,19]. In contrast, for bubbles, dissipation occurs in the surrounding unbounded liquid, obscuring relevant length scales. Additionally, bubbles must overcome substantial liquid inertia [12,14,15] and adhesion energy [15], preventing direct application of droplet-based approaches, for which extensive literature exists [20–22], to bubbles. Detachment criteria for bubbles so far rely on limited experimental data [14,15], with bubbles growing on pits and no information on the contact patch evolution, and numerical investigations [13,23], where the accurate representation of the contact line remains challenging. There is no consensus on the mechanism governing the jumping/sticking transition: Refs. [13,23] propose a competition between neck touchdown and contact patch removal by capillary waves, while others favor energy arguments [14,15]. For the latter, it remains unclear whether dissipation or adhesion energy dominates, and the dissipation scaling proposed in [14] is inconsistent with experimental data.

In this paper, we address these open questions and develop a criterion for bubble detachment after coalescence, incorporating material properties (density ρ , viscosity μ , surface tension σ , equilibrium contact angle θ_{eq}) and geometric parameters (bubble radius R , and contact patch radius R_{cont}). Through experiments and accompanying direct numerical simulations, we demonstrate that coalescence outcomes are primarily governed by the balance between available surface energy ΔG , adhesion energy W_a , and viscous dissipation W_μ . Using a transparent electrode reveals contact line motion during bubble coalescence, enabling a comprehensive energy balance analysis.

II. METHODS

A. Experimental details

A custom-made electrolysis cell was used for the experiments, as outlined in Fig. 1(a). The cell featured a 40 mm diameter disk electrode (cathode) comprising a 20 nm thin film of platinum (Pt) sputtered onto a microscope glass slide. A tantalum layer with 3 nm thickness applied to improve the adhesion between Pt and glass. A platinized titanium mesh served as the anode, while an Ag/AgCl electrode (in 3 M NaCl; BASi®) functioned as the reference electrode. Further details on the cell and WE are given in previous works [24–26]. The electrolyte consisted of 0.1 M and 1 M perchloric acid (HClO₄) solutions. To improve the conductivity, 0.5 M sodium perchlorate monohydrate (NaClO₄·H₂O) was added to the 0.1 M solution as a supporting electrolyte. The chemicals used in the experiments were supplied from Sigma-Aldrich (purity of 99.99%). A Biologic VSP-300 potentiostat was used to perform the chronopotentiometry experiments. The applied current densities (j) are kept low ($|j| \leq 200$ A/m²), such that potential thermal [27] or solutal [28] Marangoni effects or electrostatic forces remain negligible [26].

The thin layer of platinum deposited on the glass substrate provides optical transparency to the working electrode, allowing for high-resolution visualization and analysis of the bubbles from underneath [see Fig. 1(a)]. Bubbles were monitored by a high-speed camera (Photron Nova S12) with

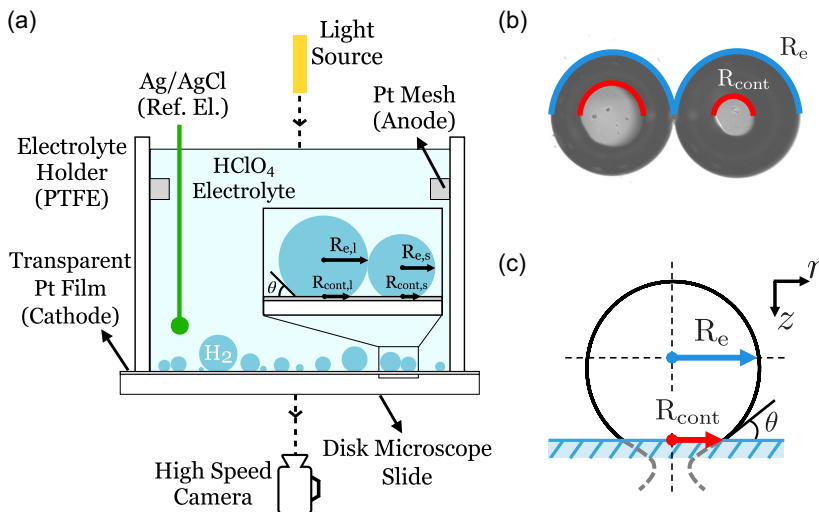


FIG. 1. (a) Schematic of the shadowgraphy setup for observing the coalescence of wall-attached bubbles. (b) Typical experimental image of coalescing bubbles, used to determine R_{cont} and R_e (indicated by half-circles). (c) Reconstructed bubble shape based on the Young-Laplace equation and the measured values of R_{cont} and R_e .

frame rates between 10 Hz and 50 000 Hz, employing a $5\times$ magnification objective lens (Olympus MPLFLN) and backlight illumination. The calibration procedure was explained in a previous work [26]. From the resulting images [see Fig. 1(b)], we extract the equatorial radii $R_{e,i}$ [with subscript $i = l, s$ denoting the large (l) or the small (s) bubble] based on the black regions and the contact patch radii $R_{cont,i}$ from the central gray areas. Bubbles with identical $R_{e,i}$ can differ in volume due to variations in $R_{cont,i}$. Therefore, we use the volume equivalent radius R_i to characterize the bubble size. To obtain R_i along with the contact angle θ , we solve the Young-Laplace equations [29] for the bubble shape [see Fig. 1(c)], assuming rotational symmetry with $R_{cont,i}$ and $R_{e,i}$ as constraints [26]. These shapes also provide the initial conditions for our volume-of-fluid based direct numerical simulations (DNS), performed using the open-source Basilisk C language [30–32].

B. Governing equations and numerical setup

To further elucidate the dynamics of coalescence-induced bubble jumping, we use the volume of fluid (VoF) based finite volume method implemented in the open-source software Basilisk C [30,31]. This approach solves the mass and momentum conservation equations given by

$$\tilde{\nabla} \cdot \tilde{\mathbf{v}} = 0, \quad (1)$$

$$\frac{\partial \tilde{\mathbf{v}}}{\partial \tilde{t}} + \tilde{\nabla} \cdot (\tilde{\mathbf{v}} \tilde{\mathbf{v}}) = \frac{1}{\rho^*} (-\tilde{\nabla} \tilde{p}' + \tilde{\nabla} \cdot (2Oh^* \tilde{\mathcal{D}}) + \mathbf{f}_\delta), \quad (2)$$

where lengths are normalized by the pre-coalescence single bubble radius. The velocity \mathbf{v} and pressure p are normalized using the inertio-capillary velocity $U_\sigma = \sqrt{\sigma/\rho_l R}$ and capillary pressure $P_\sigma = \sigma/R$, respectively. Note that, in the simulations, we only focus on the symmetric bubbles $R_l = R_s = R$. Here, \mathcal{D} represents the symmetric part of the velocity gradient tensor, and \mathbf{f}_δ is the singular body force at the liquid-gas interface. Following [33], we redefine pressure as $\tilde{p}' = \tilde{p} + Bo \tilde{\rho} \tilde{z}$, where the Bond number, $Bo = \rho g R^2 / \sigma$, compares gravitational and capillary pressures. The singular body force is given by

$$\mathbf{f}_\delta \approx \left(\tilde{\kappa} + Bo \left(1 - \frac{\rho_{\text{gas}}}{\rho} \right) \tilde{z} \right) \tilde{\nabla} \Psi, \quad (3)$$

with Ψ as the volume of fluid (VoF) color function distinguishing liquid ($\Psi = 1$) from gas ($\Psi = 0$). Using the one-fluid approximation [34], we express the Ohnesorge number Oh^* and dimensionless density $\tilde{\rho}^*$ as

$$Oh^* = Oh \left(\Psi + (1 - \Psi) \left(\frac{\mu_{\text{gas}}}{\mu} \right) \right), \quad (4)$$

$$\tilde{\rho}^* = \Psi + (1 - \Psi) \left(\frac{\rho_{\text{gas}}}{\rho} \right), \quad (5)$$

where μ_{g}/μ and ρ_{g}/ρ are gas-liquid viscosity and density ratios, respectively. The liquid Ohnesorge number is defined as

$$Oh = \frac{\mu}{\sqrt{\rho\sigma R}}. \quad (6)$$

To streamline our investigation, we fix ρ_{gas}/ρ at 7.82×10^{-5} and μ_{gas}/μ at 8.8×10^{-3} , reflecting realistic hydrogen properties. We maintain Oh at 7.5×10^{-3} for all cases except those directly comparing with experiments. Furthermore, we employ the simplest contact line model where we prescribe the contact angle θ_{eq} in the first computational cell adjacent to the electrode. A numerical slip regularizes the well-known contact line singularity [35,36]. For detailed methodology and the Basilisk C codes to solve the above equations, we refer readers to [32].

III. RESULTS AND DISCUSSION

Based on the bubble parameters along with the material properties of the electrolyte and hydrogen, we can estimate the released surface energy $\Delta G \sim \sigma(R_l^2 + R_s^2 - R_m^2)$ where $R_m = (R_l^3 + R_s^3)^{1/3}$ is the volume equivalent radius of the merged bubble, and the total adhesion energy $W_{a,\text{tot}} \sim \sigma \cos \theta_{eq}(R_{\text{cont},l}^2 + R_{\text{cont},s}^2)$, based on which we define the dimensionless adhesion energy,

$$W_{a,\text{tot}}^* \equiv \frac{\cos \theta_{eq}(R_{\text{cont},l}^2 + R_{\text{cont},s}^2)}{R_l^2 + R_s^2 - R_m^2}, \quad (7)$$

as a control parameter. Here, the equilibrium contact angle θ_{eq} characterizes the surface wettability, which directly determines the adhesion force between the bubble and the solid surface. Additionally, the system features three more dimensionless control parameters, namely the Ohnesorge number Oh (dimensionless electrolyte viscosity), the radius ratio $x \equiv R_l/R_s$, and the Bond number Bo (dimensionless gravity).

A. Key observations for $x \approx 1$

Figure 2 demonstrates the coalescence of two similarly sized bubbles ($R_l \approx R_s = R$) through experimental bottom-view grayscale images and numerical simulations. Time $t^* = t/\tau$ is normalized using the inertio-capillary timescale $\tau = \sqrt{\rho R^3/\sigma}$ [37]. The numerical results for two identical bubbles, represented by orange outlines overlaid on the experimental images and three-dimensional renderings, show remarkable agreement with the experiments. This confirms that potential additional factors, such as contact line hysteresis, electric forces, and Marangoni stresses—neglected in the simulations—are of only secondary importance in the present problem. As the bubbles merge, a neck forms between them, expanding rapidly due to the strong Laplace pressure ($\Delta P \sim \sigma R/r_n^2$), where r_n is the neck radius [16,18,38]. This expansion follows the established scaling $r_n \sim t^{1/2}$ (not shown), resulting from the hydrodynamic singularity at the intersection of two spherical bubbles [37]. Initially, the neck expands symmetrically in the radial direction (Fig. 2, $t^* \approx 0.01$ – 0.33). Subsequently, the presence of the wall breaks this symmetry (Fig. 2, $t^* \approx 0.5$, see also [12]). Importantly, the lower neck never contacts the wall during coalescence, presumably due to the strong lubrication pressure between the neck and the surface. The experimental images clearly show the contact lines of both bubbles, confirming the presence of this gap. This holds true irrespective of

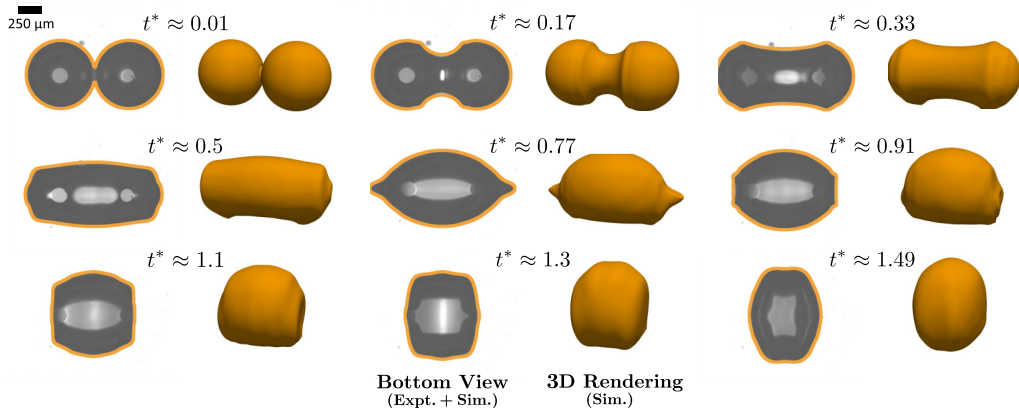


FIG. 2. Shape and contact line evolution of two coalescing bubbles on a surface comparing experiment and simulations. Each pair shows (left) experimental bottom view (grayscale) overlaid with numerical simulation contour (orange), and (right) 3D rendering from numerical simulation. In the experiments, $R_l \approx 323 \mu\text{m}$, $R_s \approx 321 \mu\text{m}$, $R_{\text{cont},l} = 59 \mu\text{m}$, and $R_{\text{cont},s} = 72 \mu\text{m}$. In the simulations, $R = 322 \mu\text{m}$ and $R_{\text{cont}} = 59 \mu\text{m}$. $Oh = 0.0066$, $Bo = 0.016$, and $W_{a,\text{tot}}^* \approx 0.07$. See the full movie in the Supplemental Material.

whether the coalescence event results in detachment [as is the case in Fig. 1(b), or not (see Figs. 6 and S1)]. This scenario is at odds with the simulation results of [13], who identified the touchdown of the neck and the resulting enlargement of the contact patch as the key effect resisting bubble departure.

Following the neck expansion, capillary waves emerge and propagate along the bubble surfaces, significantly altering their shape. For (nearly) identically sized bubbles, waves converge at the two apices simultaneously, generating a characteristic lemonlike shape at $t^* \approx 0.77$ (Fig. 2). Subsequently, surface tension drives a retraction wave inwards (Fig. 2, $t^* \approx 0.91$), initiating contact line motion from the outer edge at $t^* \approx 1.1$. The presence of contact angle hysteresis in the experiments ($\approx 70^\circ$ despite low mean roughness $\approx 1 \text{ nm}$ [26]) ensures that the contact line of both bubbles remains pinned until the waves return to the contact line [39,40]. When capillary waves reach the contact line, either the entire contact patch is swept away, leading to bubble detachment (as observed at $t^* \approx 1.49$ in Fig. 2), or the bubble remains stuck to the surface. In the latter case, the smaller of the two contact patches typically still gets peeled off, but the larger patch remains attached retaining the bubble. This is particularly evident from Fig. 7, which shows that the contact area after coalescence ($A_{\text{cont},m}$) is usually close to the one of the larger patch ($A_{\text{cont},lp}$) before the event, especially as $x \gtrsim 1.8$. Note that the larger patch, denoted with subscript "lp," is typically but not exclusively associated with the larger bubble. Persistent shape oscillations after coalescence modulate the contact patch size of the sticking bubble after the event in some instances. Only for rare cases at $x \approx 1$, we observe a “moving contact patch,” where both contact areas converge and merge at the bubbles’ center (see Sec. S1 of [41]).

Figure 3 summarizes the coalescence outcomes for the symmetrical case with $x \approx 1$ across a range of Bo and $W_{a,\text{tot}}^*$ values, comparing simulations (orange squares) and experiments (red circles). Empty markers denote jumping, while filled markers indicate sticking. Notably, the outcome exhibits only a weak dependence on Bo over two orders of magnitude of Bo ($10^{-3} < Bo < 10^{-1}$), with $W_{a,\text{tot}}^*$ emerging as the critical parameter governing the jumping-sticking transition in this regime. This transition occurs around $W_{a,\text{tot}}^* \approx 0.15$ (indicated by the gray shaded area in the plot), implying that bubbles fail to jump when adhesion energy exceeds approximately 15% of the total released surface energy (at $Oh \approx 0.0075$). The numerical results are largely consistent with this threshold despite the lack of contact line hysteresis in the simulations, indicating that this is a secondary effect. The slight trend in the jumping threshold toward higher $W_{a,\text{tot}}^*$ at the upper Bo limit visible

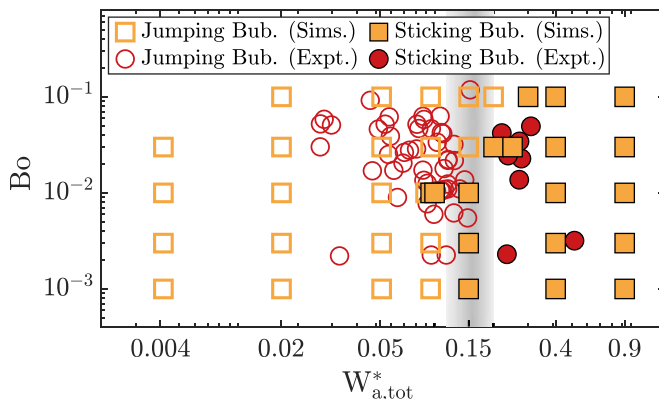


FIG. 3. Coalescence outcomes for similarly sized bubbles ($x < 1.2$ and $R_{cont,l}/R_{cont,s} < 1.2$) in the experiments (red), and identical ones in the simulations (orange) across the Bond number Bo vs dimensionless adhesion energy $W_{a,tot}^*$ phase space. Open and filled markers denote jumping and sticking cases, respectively. Gray shading marks the jumping-sticking transition region.

for the simulations may result from increased buoyancy forces favoring detachment. Overall, these results clearly demonstrate the important role the adhesion energy plays in the problem. Taking this into account, we will now extend our analysis to asymmetric coalescence events with size ratios $x > 1$.

B. Adhesion limited jumping inhibition of asymmetric bubbles

For asymmetric bubbles, the total dimensionless adhesion energy $W_{a,tot}^*$, but also its distribution between the large ($W_{a,l}^*$) and small ($W_{a,s}^*$) bubbles may influence the coalescence process. Figure 4 presents our experimental results in the $W_{a,l}^* - W_{a,s}^*$ phase space, classifying jumping and sticking bubbles. Each data point represents a coalescence event, with marker style indicating the outcome (filled symbols for sticking, open for jumping) and shade representing the bubble size ratio x . The data discussed up to now falls close to the diagonal line, denoting equal distribution of the adhesion

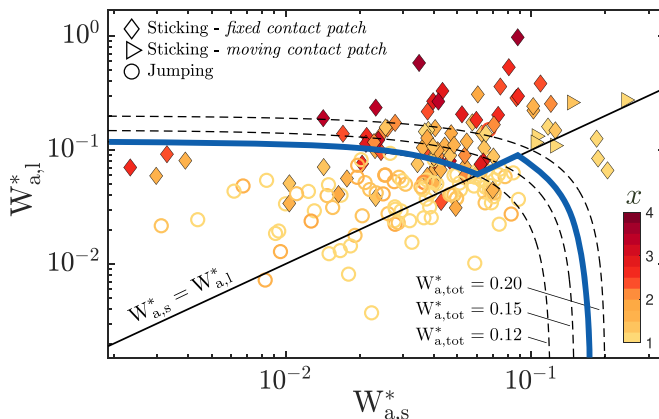


FIG. 4. Sticking (filled) and jumping (open markers) as a function of the dimensionless adhesion energies of the larger ($W_{a,l}^*$) and smaller ($W_{a,s}^*$) bubbles. The diagonal line represents $W_{a,l}^* = W_{a,s}^*$, dashed lines are isocontours of the total dimensionless adhesion energy $W_{a,tot}^*$.

energy between the bubbles, while dashed lines indicate isocontours of $W_{a,\text{tot}}^*$. Cases where the merged bubble is expected to detach due to buoyancy are omitted from the analysis (see Sec. S2 of [41]).

As expected, larger bubbles typically exhibit higher adhesion energy than smaller ones, which is reflected in the concentration of points above the diagonal. For these “regular” cases, the adhesion energy threshold for jumping inhibition $W_{a,\text{tot}}^* \approx 0.12$ is similar to that of identical bubbles ($W_{a,\text{tot}}^* \approx 0.15$). However, “irregular” cases, for which the smaller bubble has a higher adhesion energy, show jumping inhibition only at slightly higher thresholds ($W_{a,\text{tot}}^* \approx 0.15\text{--}0.20$), indicating that this configuration favors detachment. The blue solid line approximates this transition between jumping and sticking. Furthermore, a significant correlation exists between the bubble size ratio x and coalescence outcome, with larger ratios increasing the probability of sticking. The vast majority of jumping events occur for $x \lesssim 1.75$ (Fig. S3 in [41]). This observation aligns with the fact that coalescence of similarly-sized bubbles releases more energy than that of bubbles with the same total volume but greater size disparity [14,42].

C. Global energy balance

The fate of the merged bubble—whether it jumps or remains stuck—can be predicted by the global energy balance in a coalescence event. The surface energy released during bubble coalescence ΔG , resulting from the reduced gas-liquid interfacial area, is transformed into energy overcoming adhesion forces $W_{a,\text{tot}}$, viscous dissipation W_μ , change in potential energy ΔE_{pot} , and translational kinetic energy E_{kin} if the merged bubble detaches. ΔE_{pot} results from the slight shift in the center of mass of the bubbles before and after coalescence and is negligible compared to ΔG . E_{kin} constitutes a minor fraction of the total released energy across all investigated cases (see Appendix B). The jumping-sticking transition is defined by $E_{\text{kin}} \approx 0$. Consequently, the global energy balance for this case yields

$$\Delta G = W_{a,\text{tot}} + W_\mu. \quad (8)$$

For the viscous dissipation due to the velocity gradients generated in the surrounding liquid during coalescence, we derive the scaling

$$W_\mu \sim \mu_{\text{gas}} \sqrt{\sigma / \rho} R_m^{3/2}, \quad (9)$$

with details provided in Appendix C. We emphasize that the dissipation primarily occurs in the liquid and μ_{gas} only enters in Eq. (9) through the interface continuity condition. Inserting the respective scaling relations for the terms in Eq. (8) and normalizing by ΔG results in

$$\alpha_1 W_{a,\text{tot}}^* + \alpha_2 W_\mu^* = 1, \quad (10)$$

with the dimensionless adhesion energy $W_{a,\text{tot}}^*$ [see Eq. (7)] and the normalized viscous dissipation

$$W_\mu^* \equiv \frac{\mu_{\text{gas}} \sqrt{\sigma / \rho} R_m^{3/2}}{\sigma (R_l^2 + R_s^2 - R_m^2)}. \quad (11)$$

The parameters α_1 and α_2 account for the transition from exact balance to scaling relations. Volume conservation during coalescence implies $R_m = (1 + x^3)^{1/3} R_s$, allowing W_μ^* to be expressed as an effective Ohnesorge number $W_\mu^* = (\mu_{\text{gas}} / \mu) \cdot Oh \cdot f(x)$, where

$$f(x) = \frac{\sqrt{x(1+x^3)}}{x^2 + 1 - (1+x^3)^{2/3}} \quad (12)$$

depends solely on the radius ratio x , which acts to increase the effective Ohnesorge number for asymmetric coalescence events (see Fig. 9).

Figure 5 presents the data in the $W_{a,\text{tot}}^* - W_\mu^*$ parameter space of Eq. (10). To complement the present dataset, we also include data from the experiments by Lv *et al.* [14] here. In their case,

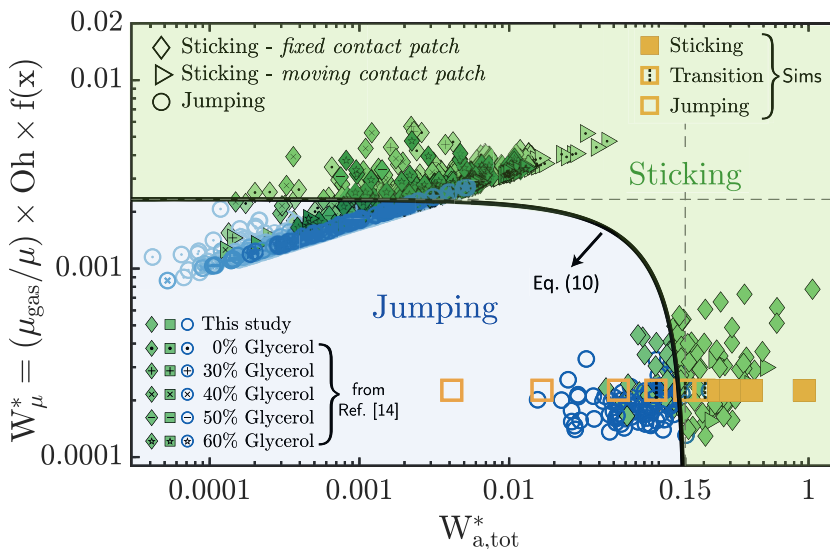


FIG. 5. Generalized detachment prediction model for coalescing wall-attached bubbles. Data from two different experimental setups are included: small bubbles (up to $\approx 150 \mu\text{m}$) with pinned contact line (upper left part, taken from Ref. [14]) and larger bubbles (up to $\approx 1250 \mu\text{m}$) with spreading contact line (lower right part, our experiments). Simulation results correspond to those in Fig. 3. The black curve depicts the best fit threshold curve base on Eq. (10). The asymptote values, $W_{a,\text{tot}}^* \approx 0.150$ and $W_{\mu}^* \approx 0.00233$ are shown as vertical and horizontal dashed lines, respectively. See Sec. S4 of [41] for the details of parameters investigated in the plot.

oxygen bubbles are formed by a catalytic reaction in H_2O_2 solution on an Au surface with contact lines pinned at predefined pits. The pits have radii of $1 \mu\text{m}$, which is the value assumed as contact radius for these cases.

Varying amounts of glycerol are added to change the liquid parameters and in particular the viscosity μ , which is increased more than tenfold at the highest concentration. The resulting bubbles are significantly smaller (≈ 10 times in size and ≈ 100 times in contact patch) than those in our experiments, which provides access to an entirely different region of the parameter space. To determine the prefactors α_1 and α_2 in Eq. (10), we seek the parameter combination that yields the largest share of correct attributions of "jumping" and "sticking" cases for both datasets. Doing so results in $\alpha_1 = 6.66$ and $\alpha_2 = 429.2$, for which $\approx 88\%$ of the total number of events is predicted successfully. The corresponding jumping-sticking transition curve based on Eq. (10) is included as a black line in Fig. 5.

In the limit of low adhesion energy, where most of the data of [14] lies, the outcome is solely determined by dissipation and the jumping threshold in the asymptotic limit is given by $W_{\mu}^* \approx 0.00233$. In contrast, the present data falls toward the limit of small W_{μ}^* , where the fate of the bubble is determined by adhesion with a critical value of $W_{a,\text{tot}}^* \approx 0.150$ in the limit of negligible dissipation.

IV. CONCLUSIONS

In conclusion, we have shown that in addition to the viscous dissipation, the adhesion energy of surface-attached coalescing bubbles also plays a critical role in determining their fate. This is based on the direct experimental observation of the contact line dynamics during coalescence and consistent with numerical simulations at matched conditions. By evaluating the energy balance at the sticking-jumping transition, we derived a detachment criterion that captures and is consistent

with all available data on this problem. One of the two relevant input parameters is an effective Ohnesorge number, that accounts for size disparity and the gas-liquid viscosity ratio. The other parameter is the dimensionless adhesion energy, which can be related to the contact angle when evaluating the criterion for a particular bubble configuration. The developed expression has strong support with data spanning several orders of magnitude in both parameters, and can be used, e.g., to optimize surface structures of electrodes or boilers to enhance bubble release. Note that the criterion developed here features no dependence on electrolyte properties other than θ_{eq} . At least for the numerically accessible parameter range, this is supported by the agreement with the simulations, for which potential electrolyte dependent effects such as Marangoni stresses are absent.

ACKNOWLEDGMENTS

We thank Pengyu Lv for providing the original data in his study. We also thank Andrea Prosperetti and Wilko Rohlf's for stimulating discussions. This research was supported by the Dutch Research Council (NWO) through the ENW PPP Fund for top sectors, with contributions from Shell, Nobian, and Nouryon and the Ministry of Economic Affairs via the PPS-toeslagregeling, Grant No. 741.019.201. Additional funding was provided by the FIP-II project, sponsored by NWO and Canon, and the European Research Council (ERC) under the European Union's Horizon 2020 research and innovation programme (Grant Agreement No. 950111, BU-PACT). We also acknowledge support from the ERC Advanced Grant MultiMelt (No. 101094492). The numerical simulations were carried out on the national e-infrastructure of SURFsara, a subsidiary of SURF cooperation, the collaborative ICT organization for Dutch education and research.

DATA AVAILABILITY

The data that support the findings of this article are openly available [43].

APPENDIX A: STICKING BUBBLES

The shape deformation and contact line motion during the coalescence of two bubbles of similar size, whose coalescence results in sticking, are shown in Fig. 6. Similar to the coalescence-induced jumping shown in Fig. 2, the neck formed during coalescence does not touch the electrode surface throughout the process. The smaller (right) contact patch becomes detached after $t^* \approx 1$, while the larger (left) patch, and consequently the merged bubble, remain attached.

Figure 7 illustrates how the contact area of the fixed bubbles changes due to the coalescence events, with respect to the size ratio x of the coalescing bubbles. The relative change in contact area is expressed as the ratio of the merged bubble's contact area after coalescence ($A_{\text{cont,m}}$) to the contact area of the bubble with the larger patch size prior to coalescence ($A_{\text{cont,lp}}$). This reference is warranted by the observation that, during coalescence, the bubble with a larger contact area predominantly remains fixed to the surface, as seen in Fig. 6. In the vast majority of cases (>96%), the bubbles whose patch remains fixed is the larger one in the coalescing pair. Figure 7 shows that for most cases $A_{\text{cont,m}}/A_{\text{cont,lp}} \approx 1$, implying that the patch size after coalescence equals the larger one prior to it. A few exceptions to this occur for $x \lesssim 1.8$, where the patch size increases slightly relative to $A_{\text{cont,lp}}$, especially when $R_{l,p}$ is comparatively small. Conversely, some cases with large $R_{l,p}$ also exhibit a decrease in patch size.

APPENDIX B: ENERGETICS OF JUMPING BUBBLES

In Figs. 8(a)–8(c), we plot the temporal evolution of the kinetic energy normalized by the total surface energy:

$$E_{\text{cm}}^* = \frac{\frac{1}{2} C_M \rho_l \frac{4}{3} \pi R_m^3 V_{\text{cm}}^2}{4\pi\sigma(R_l^2 + R_s^2 - R_m^2)} = \frac{1}{3(2 - 2^{\frac{2}{3}})} C_M V_{\text{cm}}^{*2}, \quad (\text{B1})$$

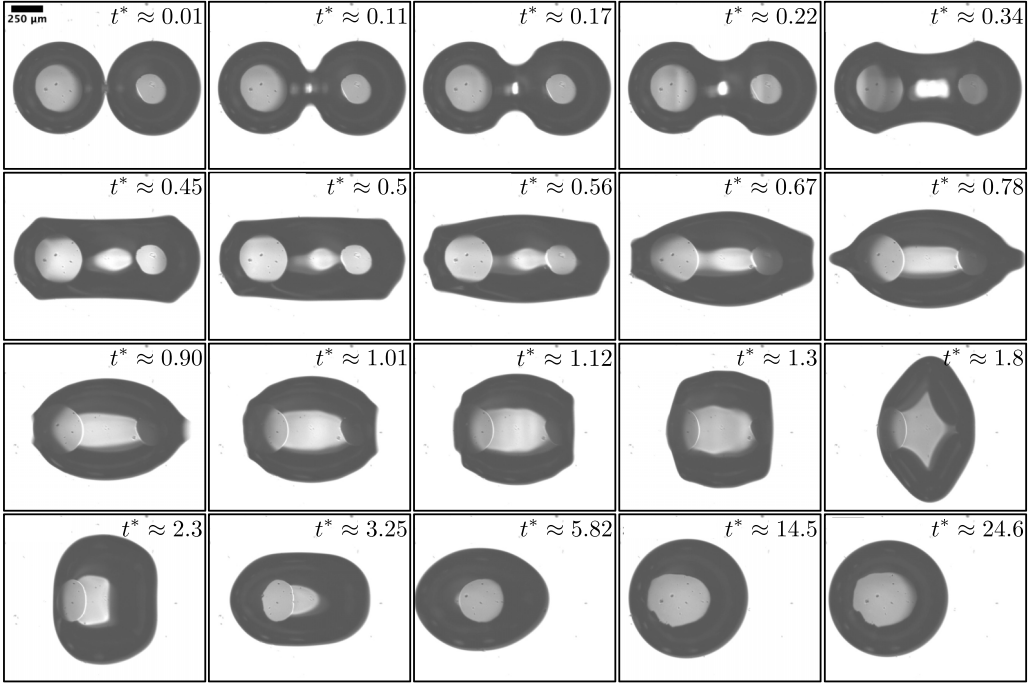


FIG. 6. Outline and contact patch of coalescing bubbles on a planar electrode recorded at 20 000 frames per second. The merged bubble keeps sticking at the electrode surface after coalescence. The parameters are $R_l \approx 371 \mu\text{m}$, $R_s \approx 360 \mu\text{m}$, $R_{\text{cont},l} = 118 \mu\text{m}$ and $R_{\text{cont},s} = 189 \mu\text{m}$. $Oh = 0.0062$, $Bo = 0.021$, and $W_{a,\text{tot}}^* \approx 0.31$. See the full movie in the Supplemental Material [41].

where V_{cm} is the dimensional center of mass velocity, V_{cm}^* is the nondimensionalized center of mass velocity, and $C_M = 0.8$ is the added mass coefficient. It shows that the kinetic energy accounts for only a small part of the total energy ($<10\%$) for both $Bo = 0.1$ [Fig. 8(a)] and $Bo = 0.001$ [Fig. 8(c)]. We further plot the energy partitions, including kinetic energy, adhesion energy, potential

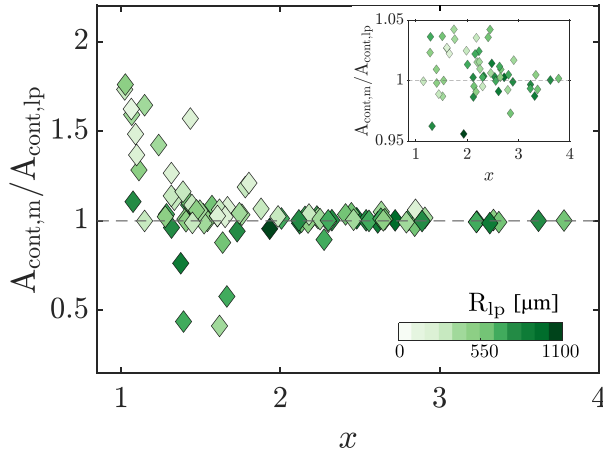


FIG. 7. Change in contact patch area of the bubble with larger contact patch ($A_{\text{cont},m}/A_{\text{cont},lp}$) with respect to the radius ratio of the coalescing bubbles (x). Color code indicates the size of bubble with larger patch (R_{lp}). The inset shows a zoomed view in the vicinity of $A_{\text{cont},m}/A_{\text{cont},lp} = 1$.

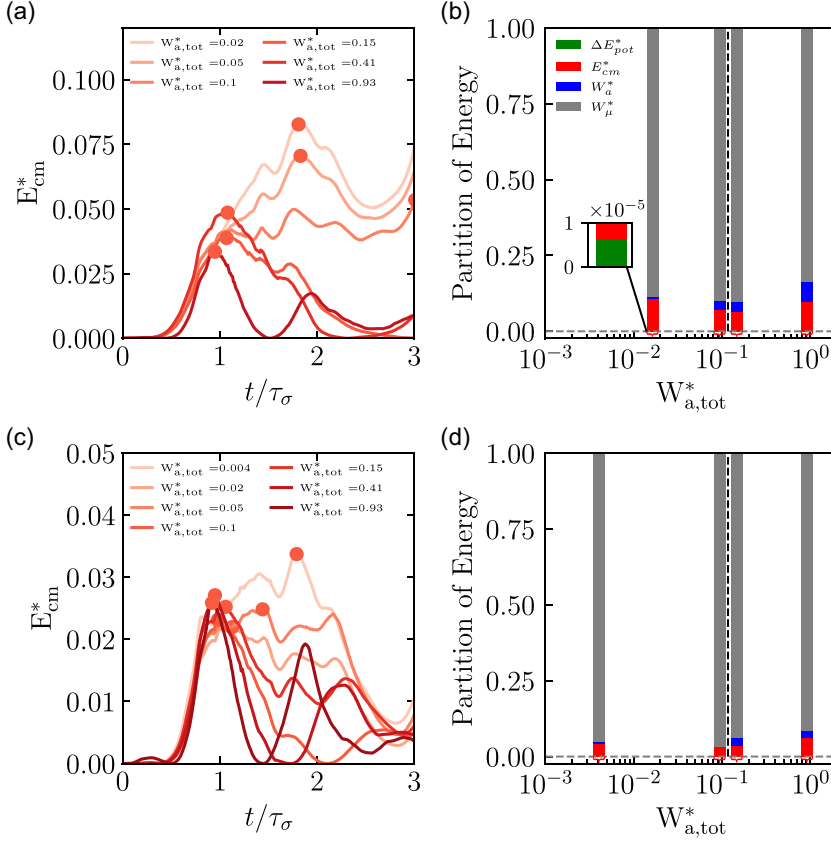


FIG. 8. (a) Kinetic energy E_{cm}^* [see Eq. (B1)] based on the center of mass velocity as a function of time for different $W_{a,tot}^*$. Here and in (b), $Bo = 0.1$. The circles represent the times when E_{cm}^* reaches the respective maximum. (b) The instantaneous energy partitions [all normalized by the instantaneous surface energy $E_s(t) - E_s(0)$] at the time when E_{cm}^* reaches the maximum for different $W_{a,tot}^*$. The green part represents the change of potential energy, the red part represents the instantaneous E_{cm}^* , the blue part represents the instantaneous adhesion energy W_a^* , and the gray part represents the remaining dissipation energy W_μ^* . The vertical dashed line shows the transition from jumping case to sticking case. (c), (d) The same plots as (a), (b) but for $Bo = 0.001$.

energy, and viscous dissipation energy (taken as the remaining energy not accounted for by the other terms here) at the time when the kinetic energy reaches its respective maximum for $Bo = 0.1$ [Fig. 8(b)] and $Bo = 0.001$ [Fig. 8(d)]. Note that the potential energy is too small to be visible in this partition plot [see blow up in Fig. 8(b)]. Analysis of the energy partitions reveals that, while most of the energy is dissipated, the adhesion energy can reach a magnitude comparable to E_{cm}^* , underscoring its significance in the problem.

APPENDIX C: SCALING RELATION FOR THE ENERGY DISSIPATION

During bubble coalescence, the dissipated energy $W_\mu(t)$ up to time t is given by the integral

$$W_\mu(t) = \int_0^t \int_V \Phi(\mathbf{x}, t') dV dt', \quad (C1)$$

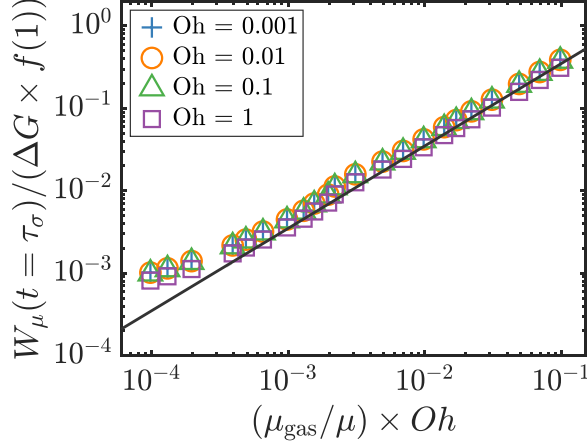


FIG. 9. Measured dissipation in the liquid over a period of τ_σ for coalescence of symmetric bubbles away from the wall with varying Oh and μ_{gas}/μ . The line represents the scaling according to Eq. (C6).

where t is time, V is the volume over which dissipation occurs, and Φ is the viscous dissipation function given by

$$\Phi(\mathbf{x}, t) = 2\mu(\mathcal{D}(\mathbf{x}, t) : \mathcal{D}(\mathbf{x}, t)). \quad (\text{C2})$$

Here, μ is the viscosity of the liquid, and the deformation tensor $\mathcal{D} = (\nabla \mathbf{v}(\mathbf{x}, t) + (\nabla \mathbf{v}(\mathbf{x}, t))^T)/2$ is the symmetric part of the velocity gradient tensor. The coalescence-induced jumping phenomenon is primarily driven by capillary stresses. Following [14,44], we can estimate the viscous dissipation Φ to leading order as

$$\Phi \sim \mu \frac{U_\sigma^2}{\lambda^2}, \quad (\text{C3})$$

where $U_\sigma \sim \sqrt{\sigma/\rho R_m}$ represents the inertio-capillary velocity. Here, R_m , the radius of the merged bubble, serves as the relevant length scale for the driving capillary stresses, and λ denotes the length scale over which velocity gradients persist in the liquid. The continuity of velocity and viscous stresses across the gas-liquid interface dictates

$$\mu \frac{U_\sigma}{\lambda} \sim \mu_{\text{gas}} \frac{U_\sigma}{R_m}, \quad (\text{C4})$$

implying that the unknown velocity gradients in the liquid can be approximated by those inside the merged bubble. We can then estimate the viscous dissipation function as $\Phi \sim \mu_{\text{gas}} U_\sigma^2 / (R_m \lambda)$, which must be integrated across the dissipation volume $V \sim \lambda R_m^2$ and over the inertio-capillary timescale of $\tau_\sigma \sim \sqrt{\rho R_m^3 / \sigma}$ to give the total viscous dissipation as

$$W_\mu \sim \mu_{\text{gas}} \sqrt{\sigma / \rho} R_m^{3/2}. \quad (\text{C5})$$

Normalizing Eq. (C5) with the released surface energy ΔG scale results in

$$\frac{W_\mu}{\Delta G} \sim \left(\frac{\mu_{\text{gas}}}{\mu} \right) \cdot Oh \cdot f(x). \quad (\text{C6})$$

This result is confirmed from simulations (see Fig. 9) and can be interpreted as an effective Ohnesorge number $(\mu_{\text{gas}}/\mu) \cdot Oh \cdot f(x)$ accounting for the viscosity ratio and size disparity.

Note that the expression derived in [14] for the same quantity amounts to setting $\lambda \approx R_m$, which yields $W_\mu \propto \mu$. However, this viscosity dependence is inconsistent with the experimental

data in Ref. [14], in which it is argued that this discrepancy may be due to an (unaccounted) viscous damping effect that effectively cancels the μ dependence for W_μ . The present formulation is consistent with the experimental data (see Fig. 4) without such an *ad hoc* assumption. We emphasize that though μ_{gas} enters into Eq. (C5) via the continuity condition Eq. (C4), the relevant dissipation of energy occurs in the liquid.

-
- [1] L. Deike, Mass transfer at the ocean–atmosphere interface: The role of wave breaking, droplets, and bubbles, *Annu. Rev. Fluid Mech.* **54**, 191 (2022).
 - [2] X. Jiang, L. Rotily, E. Villermaux, and X. Wang, Abyss aerosols: Drop production from underwater bubble collisions, *Phys. Rev. Lett.* **133**, 024001 (2024).
 - [3] T. B. Low and R. List, Collision, coalescence and breakup of raindrops. Part I: Experimentally established coalescence efficiencies and fragment size distributions in breakup, *J. Atmos. Sci.* **39**, 1591 (1982).
 - [4] M. Schlüter, S. Herres-Pawlis, U. Nieken, U. Tuttlies, and D. Bothe, Small-scale phenomena in reactive bubbly flows: Experiments, numerical modeling, and applications, *Annu. Rev. Chem. Biomol. Eng.* **12**, 625 (2021).
 - [5] J. Xu, X. Ji, W. Zhang, and G. Liu, Pool boiling heat transfer of ultra-light copper foam with open cells, *Int. J. Multiphase Flow* **34**, 1008 (2008).
 - [6] M. Wang, Z. Wang, X. Gong, and Z. Guo, The intensification technologies to water electrolysis for hydrogen production—a review, *Renew. Sustain. Energy Rev.* **29**, 573 (2014).
 - [7] C.-C. Wang, C.-Y. Chen *et al.*, Water electrolysis in the presence of an ultrasonic field, *Electrochim. Acta* **54**, 3877 (2009).
 - [8] X. Zhao, H. Ren, and L. Luo, Gas bubbles in electrochemical gas evolution reactions, *Langmuir* **35**, 5392 (2019).
 - [9] G. F. Swiegers, R. N. Terrett, G. Tsekouras, T. Tsuzuki, R. J. Pace, and R. Stranger, The prospects of developing a highly energy-efficient water electrolyser by eliminating or mitigating bubble effects, *Sustain. Energy Fuels* **5**, 1280 (2021).
 - [10] A. Angulo, P. van der Linde, H. Gardeniers, M. Modestino, and D. F. Rivas, Influence of bubbles on the energy conversion efficiency of electrochemical reactors, *Joule* **4**, 555 (2020).
 - [11] F. Sepahi, N. Pande, K. L. Chong, G. Mul, R. Verzicco, D. Lohse, B. T. Mei, and D. Krug, The effect of buoyancy driven convection on the growth and dissolution of bubbles on electrodes, *Electrochim. Acta* **403**, 139616 (2022).
 - [12] Á. M. Soto, T. Maddalena, A. Fraters, D. van der Meer, and D. Lohse, Coalescence of diffusively growing gas bubbles, *J. Fluid Mech.* **846**, 143 (2018).
 - [13] R. Iwata, L. Zhang, Z. Lu, S. Gong, J. Du, and E. N. Wang, How coalescing bubbles depart from a wall, *Langmuir* **38**, 4371 (2022).
 - [14] P. Lv, P. Peñas, H. Le The, J. Eijkel, A. van den Berg, X. Zhang, and D. Lohse, Self-propelled detachment upon coalescence of surface bubbles, *Phys. Rev. Lett.* **127**, 235501 (2021).
 - [15] H. Park, S. F. Ahmadi, T. P. Foulkes, and J. B. Boreyko, Coalescence-induced jumping bubbles during pool boiling, *Adv. Funct. Mater.* **34**, 2312088 (2024).
 - [16] M. Q. Raza, M. v. Köckritz, J. Sebilliau, C. Colin, M. Zupancic, M. Bucci, T. Troha, and I. Golobic, Coalescence-induced jumping of bubbles in shear flow in microgravity, *Phys. Fluids* **35**, 023333 (2023).
 - [17] A. Bashkatov, S. Park, Ç. Demirkir, J. A. Wood, M. T. M. Koper, D. Lohse, and D. Krug, Performance enhancement of electrocatalytic hydrogen evolution through coalescence-induced bubble dynamics, *J. Am. Chem. Soc.* **146**, 10177 (2024).
 - [18] J. D. Paulsen, R. Carmigniani, A. Kannan, J. C. Burton, and S. R. Nagel, Coalescence of bubbles and drops in an outer fluid, *Nat. Commun.* **5**, 3182 (2014).
 - [19] I. U. Vakarelski, F. Kamoliddinov, and S. T. Thoroddsen, Why bubbles coalesce faster than droplets: The effects of interface mobility and surface charge, *Langmuir* **40**, 11340 (2024).

- [20] F. Liu, G. Ghigliotti, J. J. Feng, and C.-H. Chen, Numerical simulations of self-propelled jumping upon drop coalescence on non-wetting surfaces, *J. Fluid Mech.* **752**, 39 (2014).
- [21] J. Wasserfall, P. Figueiredo, R. Kneer, W. Rohlf, and P. Pischke, Coalescence-induced droplet jumping on superhydrophobic surfaces: Effects of droplet mismatch, *Phys. Rev. Fluids* **2**, 123601 (2017).
- [22] X. X. Yan, L. L. Zhang, S. S. Sett, L. L. Feng, C. C. Zhao, Z. Z. Huang, H. H. Vahabi, A. K. Kota, F. F. Chen, and N. N. Miljkovic, Droplet jumping: Effects of droplet size, surface structure, pinning, and liquid properties, *ACS Nano* **13**, 1309 (2019).
- [23] P. Zhao, Z. Hu, P. Cheng, R. Huang, and S. Gong, Coalescence-induced bubble departure: Effects of dynamic contact angles, *Langmuir* **38**, 10558 (2022).
- [24] N. Pande, S. K. Chandrasekar, D. Lohse, G. Mul, J. A. Wood, B. T. Mei, and D. Krug, Electrochemically induced pH change: Time-resolved confocal fluorescence microscopy measurements and comparison with numerical model, *J. Phys. Chem. Lett.* **11**, 7042 (2020).
- [25] N. Pande, J. A. Wood, G. Mul, D. Lohse, B. T. Mei, and D. Krug, Electroconvective instability in water electrolysis: An evaluation of electroconvective patterns and their onset features, *Phys. Rev. Appl.* **16**, 034021 (2021).
- [26] Ç. Demirkir, J. A. Wood, D. Lohse, and D. Krug, Life beyond fritz: On the detachment of electrolytic bubbles, *Langmuir* **40**, 20474 (2024).
- [27] J. Massing, G. Mutschke, D. Baczymalski, S. S. Hossain, X. Yang, K. Eckert, and C. Cierpka, Thermo-capillary convection during hydrogen evolution at microelectrodes, *Electrochim. Acta* **297**, 929 (2019).
- [28] S. Park, L. Liu, Ç. Demirkir, O. van der Heijden, D. Lohse, D. Krug, and M. T. Koper, Solutal marangoni effect determines bubble dynamics during electrocatalytic hydrogen evolution, *Nat. Chem.* **15**, 1532 (2023).
- [29] A. K. Chesters, Modes of bubble growth in the slow-formation regime of nucleate pool boiling, *Int. J. Multiphase Flow* **4**, 279 (1978).
- [30] S. Popinet, An accurate adaptive solver for surface-tension-driven interfacial flows, *J. Comput. Phys.* **228**, 5838 (2009).
- [31] S. Popinet and collaborators, Basilisk C, <http://basilisk.fr>.
- [32] V. Sanjay and R. Yang, Jumping bubbles: A computational framework for studying bubble coalescence, <https://comphy-lab.org/JumpingBubbles/>.
- [33] S. Popinet, Numerical models of surface tension, *Annu. Rev. Fluid Mech.* **50**, 49 (2018).
- [34] G. Tryggvason, R. Scardovelli, and S. Zaleski, *Direct Numerical Simulations of Gas-Liquid Multiphase Flows* (Cambridge University Press, Cambridge, UK, 2011).
- [35] S. Afkhami, J. Buongiorno, A. Guion, S. Popinet, Y. Saade, R. Scardovelli, and S. Zaleski, Transition in a numerical model of contact line dynamics and forced dewetting, *J. Comput. Phys.* **374**, 1061 (2018).
- [36] J. H. Snoeijer and B. Andreotti, Moving contact lines: Scales, regimes, and dynamical transitions, *Annu. Rev. Fluid Mech.* **45**, 269 (2013).
- [37] J. Eggers, J. E. Sprittles, and J. H. Snoeijer, Coalescence dynamics, *Annu. Rev. Fluid Mech.* **57** (2024).
- [38] A. T. Oratis, V. Bertin, and J. H. Snoeijer, Coalescence of bubbles in a viscoelastic liquid, *Phys. Rev. Fluids* **8**, 083603 (2023).
- [39] K. L. Mittal, *Contact Angle, Wettability and Adhesion* (CRC Press, 2003), Vol. 3.
- [40] S.-J. Hong, F.-M. Chang, T.-H. Chou, S. H. Chan, Y.-J. Sheng, and H.-K. Tsao, Anomalous contact angle hysteresis of a captive bubble: Advancing contact line pinning, *Langmuir* **27**, 6890 (2011).
- [41] See Supplemental Material at <http://link.aps.org/supplemental/10.1103/nq3w-57gg> for the details of moving contact patch, buoyancy-driven departures, a comment on bubble size ratio relationship to adhesion energy, and the details of parameters investigated, which includes Refs. [45,46].
- [42] A. Bashkatov, F. Bürkle, Ç. Demirkir, W. Ding, V. Sanjay, A. Babich, X. Yang, G. Mutschke, J. Czarske, D. Lohse, D. Krug, L. Büttner, and K. Eckert, Electrolyte spraying within H₂ bubbles during water electrolysis under normal and microgravity conditions, *Nat. Commun.* **16**, 4580 (2025).

- [43] Ç. Demirkir, D. Krug, P. Lv, R. Yang, A. Bashkatov, V. Sanjay, D. Lohse, P. Peñas, H. Le-The, J. Eijkel, A. van den Berg, and X. Zhang, Dataset for: To jump or not to jump: Adhesion and viscous dissipation dictate the detachment of coalescing wall-attached bubbles, <https://zenodo.org/records/17566467>.
- [44] V. Sanjay, P. Chantelot, and D. Lohse, When does an impacting drop stop bouncing? *J. Fluid Mech.* **958**, A26 (2023).
- [45] L. Korson, W. Drost-Hansen, and F. J. Millero, Viscosity of water at various temperatures, *J. Phys. Chem.* **73**, 34 (1969).
- [46] L. H. Brickwedde, Properties of aqueous solutions of perchloric acid, *J. Res. Natl. Bur. Stan.* **42**, 309 (1949).